



QUANTITATIVE CHARACTERIZATION AND MODELING OF COMPOSITE MICROSTRUCTURES BY VORONOI CELLS

SOMNATH GHOSH, ZDZISLAW NOWAK[†] and KYUNGHOOON LEE

Department of Aerospace Engineering, Applied Mechanics and Aviation, The Ohio State University, Columbus, OH 43210, U.S.A.

(Received 8 July 1996; accepted 10 October 1996)

Abstract—In this paper, Voronoi cells resulting from Dirichlet tessellation of a planar heterogeneous microstructure are introduced as a unified tool in characterization and response modeling of multiphase materials. Microstructures with different volume fractions, inclusion concentrations and patterns are computer simulated, and tessellated to yield a mesh of Voronoi cells. Various characterization functions of Voronoi cell based geometric parameters are generated. The Voronoi cell finite element method (VCFEM) is executed for plane strain analysis of the microstructures. These results are used for comparing measures of geometric and mechanical anisotropy, and for evaluating statistical functions of stresses.

© 1997 Acta Metallurgica Inc.

1. INTRODUCTION

Advanced materials like particle/fiber reinforced composite materials can improve systems reliability and reduce life-cycle costs in many engineering systems through enhanced thermal and mechanical performance and weight reduction. The degree of property enhancements depends on the size, shape and properties of the second phase, as well as on their spatial distribution within the matrix. It is established that though the overall elastic response is relatively less sensitive to the microstructural morphology, plastic behavior is highly affected by the local configuration due to nonhomogeneous deformation of the ductile constituents. Brockenbrough *et al.* [1] have concluded that, while both the fiber shape and distribution affect transverse tensile and shear deformations at high fiber volume fractions, the effect of fiber distribution is stronger at lower volume fractions. Christman *et al.* [2] have shown that clustering has a significant effect in reducing flow stress and strain hardening, though its effect on elastic properties is minimal. Böhm *et al.* [3] have demonstrated that the overall flow stress and the strain difference between phases is dependent on the continuity of the weaker phase. Additionally, local morphology of heterogeneities have a definitive effect on failure properties like ductility, fracture toughness, fatigue, creep resistance, etc. To take advantage of the improved attributes of advanced materials and minimize failure, an understanding of the microstructure-property relationship is a necessary step in effective component fabrication, and prediction of component behavior and life.

Many analytical micromechanical models, such as those based on the variational approach [4], self-consistent schemes [5, 6] and effective mean field theories [7–10] have evolved within the framework of small deformation linear elasticity or elasto-plasticity theory. These models predominantly follow the idea of eigenstrain based equivalent inclusion methods and take into account the reinforcement volume fraction and the aspect ratio. Though reasonably effective in predicting overall material properties for relatively simple geometries at low volume fractions, these methods are incapable of depicting stress/strain variations. Arbitrary dispersions of multiple phases, encountered in many advanced materials, cannot be deterministically treated with these models. Applications of nonlinear analytical models to many real materials are even less effective than the linear models due to nonhomogeneous plastic flow. Local properties become stress dependent and the overall constitutive response is influenced by distributions and shapes of second phase. Another class of analytical model has evolved in the form of random medium theories, in which statistical *N*-point correlation functions have been used to characterize composite microstructures [11, 12]. Though novel from a stereological point of view, these models do not overcome some of the problems discussed above.

Shortcomings of analytical models have promoted the extensive use of computational unit cell models [2, 13, 14], that generate the overall material response through detailed discretization of a representative material element (RME) in the microstructure. Effective material properties are ascertained by assuming macroscopic periodicity conditions on the RMEs. The vast majority of these models also make assumptions of local periodicity, implying a uniform

[†]On leave from Polish Academy of Sciences, Warsaw, Poland.

distribution of heterogeneities to curtail computations. These simplified unit cells bear little relationship to the actual stereographic features for many materials. In recent years, Suresh and coworkers [1, 2, 15], McHugh *et al.* [16] and Böhm and co-workers [3, 17, 18] have made novel progress in modeling discontinuously reinforced materials with a random spatial dispersion. In general, large inclusion aggregates require a very high resolution finite element mesh that leads to enormous computational efforts. For some special cases, Böhm and Rammerstorfer [18] have constructed special unit cells and boundary conditions to avert large computations. Ghosh and coworkers have developed a microstructure based Voronoi Cell Finite Element Model (VCFEM) [19–23], which attempts to overcome difficulties in modeling materials with arbitrary phase dispersions. This formulation combines concepts of finite element methods with the essential requirements of micromechanics, to yield an effective material based element. The VCFEM mesh naturally evolves from the microstructure by *Dirichlet tessellation* to generate a morphology based network of multi-sided *Voronoi polygons*. In VCFEM, each Voronoi cell representing the fundamental microstructural composition is an element, and the analysis needs no further discretization. Consequently, the effort in generating a compatible microstructural model is drastically reduced. Additionally, the computational efficiency is greatly enhanced due to Voronoi cell elements being considerably larger than conventional unit cell FEM elements.

Quantitative characterization of second phase populations with automatic image analysis techniques forms an important part of comprehending microstructure–property relationship in heterogeneous materials. Pioneering work on quantitative metallography has been carried out by Richmond and coworkers [24–27], who have used Dirichlet tessellations to characterize alloy steels and aluminum matrix composites by comparing actual and computer generated idealized microstructures. More recently they have characterized three dimensional (3D) distributions simulated from actual two dimensional (2D) micrographs by pseudo-Saltykov transformation [26] and by pair correlation functions [27]. Everett and Chu [28, 29] have used the Dirichlet tessellation for determining near neighbor distances, cell volume fractions (VFs) and radial distribution functions for computer generated patterns and compared them with real materials. Pyrz [30–32] introduced novel parameters and geometric descriptors to stereologically quantify and distinguish between various nonrandom distributions to heterogeneous microstructures.

Despite progress in characterization, little has been done to formally establish the relationships between functions that link the overall material response with stereological features like the spatial distribution of location, size, shape and local VF of constituent

phases. Important contributions in this area are by Brockenbrough *et al.* [33] and by Pyrz [30, 31]. In Ref. [33] an Al–Si composite system has been tessellated for characterization and modeled by conventional finite element analysis. Analytical expressions for stress fields have been derived in Refs [30, 31] for utilization in unique *marked correlation function*, which depicts the effect of patterns on stresses.

The present paper is an attempt to introduce Voronoi cells as a unified tool in the characterization and response modeling of complex multiphase materials through Voronoi cell finite element analysis. Microstructures with different VFs, inclusion concentration and patterns are computer simulated, and tessellated to yield a mesh of Voronoi cells. Various characterization functions based on geometric parameters are generated, measures for detecting geometric and behavioral anisotropy are compared and statistical functions of different stress measures are evaluated. Voronoi cell finite element analysis is carried out for plane strain implying fiber reinforced composite microstructures.

2. MICROSTRUCTURE GENERATION AND CHARACTERIZATION

2.1. Computer generation of planar microstructures

Computer simulated artificial microstructures, which are considered to be RMEs, are generated to study the effects of reinforcement distribution, density and volume fraction on geometric and mechanical properties. Each representative microstructure is limited to a unit (1×1) square region and is assumed to consist of 25, 50 or 100 circular inclusions of uniform size. The overall inclusion volume fractions considered are 10.8%, 21.6% or 32.4%. Three different patterns of nonregular and nonrandom reinforcement dispersions are considered, resulting in a total of 27 different computer generated RMEs as depicted in Fig. 1. Classifications and methods of construction of each distribution are delineated below.

- *Hard core or Strauss model (HC)*. This model is generated as a variant of a pure random Poisson pattern through the imposition of the following two constraints: (a) no two inclusions are allowed to overlap and (b) all inclusions are completely contained within the region. The minimum permissible distance (MPD) between heterogeneities, and between heterogeneity surfaces and edges of the RME frame are prescribed to attain this restriction. This minimum distance is a function of the inclusion size and consequently of volume fraction and population. Scaled values of MPD for various distributions in the unit square frame are presented in Table 1. The inclusion diameter (ID) is first determined based on the desirable volume fraction (VF) and the number of inclusions (#INC). A random number generator is then used to disperse the

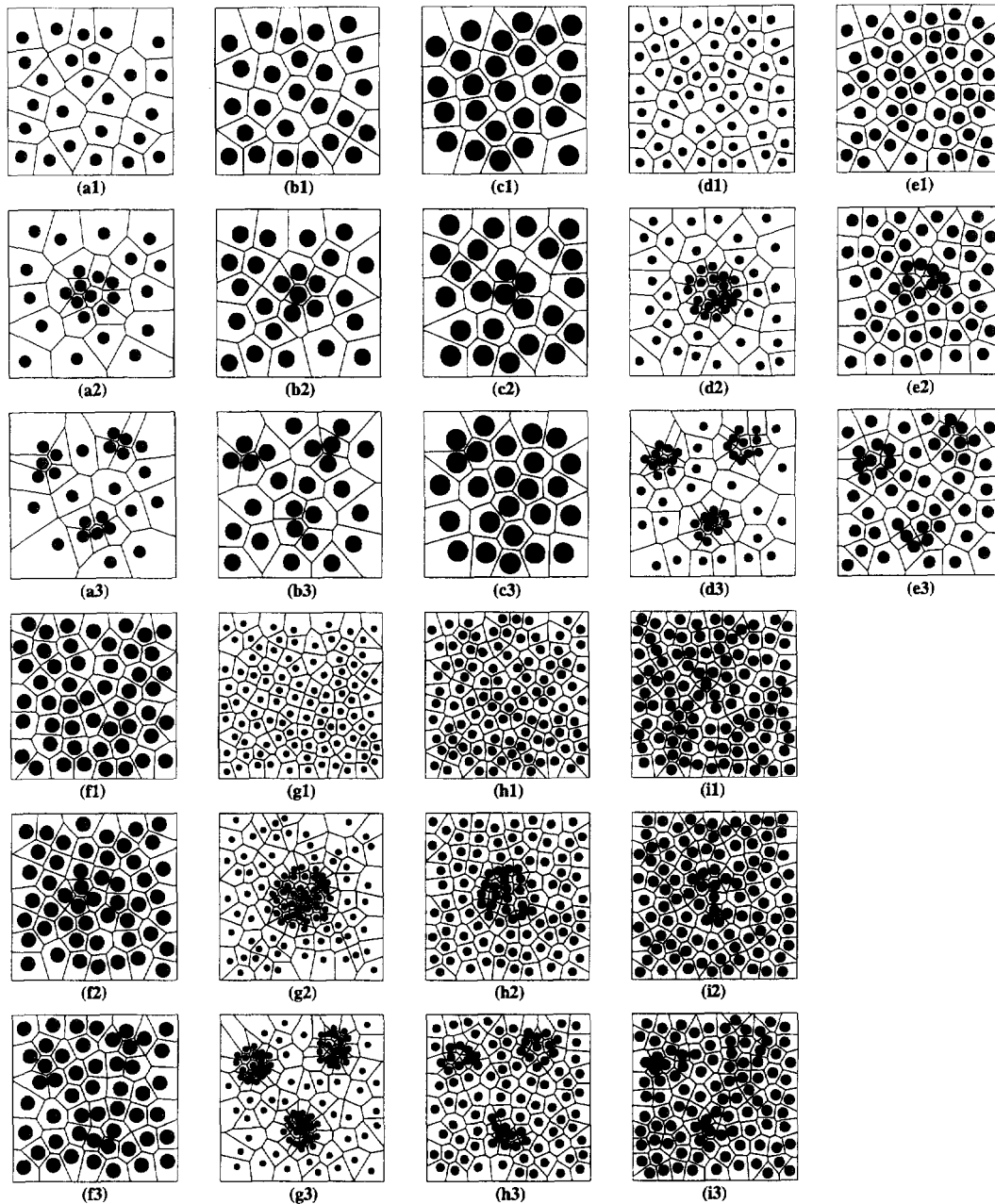


Fig. 1. Computer generated microstructures: (a) volume fraction 10.8% with 25 inclusions: (1) HC, (2) Clus-1, (3) Clus-3; (b) volume fraction 21.6% with 25 inclusions: (1) HC, (2) Clus-1, (3) Clus-3; (c) volume fraction 32.4% with 25 inclusions: (1) HC, (2) Clus-1, (3) Clus-3; (d) volume fraction 10.8% with 50 inclusions: (1) HC, (2) Clus-1, (3) Clus-3; (e) volume fraction 21.6% with 50 inclusions (1) HC, (2) Clus-1, (3) Clus-3; (f) volume fraction 32.4% with 50 inclusions: (1) HC, (2) Clus-1, (3) Clus-3; (g) volume fraction 10.8% with 100 inclusions: (1) HC, (2) Clus-1, (3) Clus-3; (h) volume fraction 21.6% with 100 inclusions: (1) HC, (2) Clus-1, (3) Clus-3; (i) volume fraction 32.4% with 100 inclusions: (1) HC, (2) Clus-1, (3) Clus-3.

inclusion centroidal locations with a predetermined value of MPD. Any event or generation that violates the MPD requirement is discarded. Too many consecutive event rejections lead to alteration of the MPD.

• *Single cluster hard core model (Clus-1)*. This model is characterized by a decreased average inclusion MPD, within a subregion of the

otherwise hardcore RME. The size (CLD), location, number of inclusions within the cluster (#INC CL) and their minimum permissible distance (MPD CL) are assessed for each representative microstructure as delineated in Table 1. An important criterion of a cluster is that the MPD CL is much smaller than the MPD as shown in Fig. 1 and Table 1.

Table 1. Various parameters used in construction of representative microstructures

VF (%)	#CL	#INC	ID	MPD	CLD	#INC CL	MPD CL
10.8	0	25	0.0742	0.0556			
10.8	0	50	0.0524	0.0524			
10.8	0	100	0.0370	0.0277			
10.8	1	25	0.0742	0.0742	0.1484	10	0.0073
10.8	1	50	0.0524	0.0524	0.1571	20	0.0026
10.8	1	100	0.0370	0.0185	0.1850	40	0.0036
10.8	3	25	0.0742	0.0742	0.0961	5	0.0036
10.8	3	50	0.0524	0.0524	0.1048	10	0.0026
10.8	3	100	0.0370	0.0370	0.1110	20	0.0018
21.6	0	25	0.1050	0.0369			
21.6	0	50	0.0742	0.0296			
21.6	0	100	0.0524	0.0183			
21.6	1	25	0.1050	0.0420	0.1313	6	0.0005
21.6	1	50	0.0742	0.0371	0.1669	12	0.0018
21.6	1	100	0.0524	0.0262	0.1702	24	0.0013
21.6	3	25	0.1050	0.0262	0.1155	4	0.0052
21.6	3	50	0.0742	0.0371	0.1289	8	0.0004
21.6	3	100	0.0524	0.0262	0.1178	12	0.0014
32.4	0	25	0.1285	0.0192			
32.4	0	50	0.0908	0.0159			
32.4	0	100	0.0642	0.0097			
32.4	1	25	0.1284	0.0224	0.1412	5	0.0003
32.4	1	50	0.0908	0.0182	0.1680	10	0.0002
32.4	1	100	0.0642	0.0129	0.1606	15	0.0016
32.4	3	25	0.1284	0.0224	0.1284	3	0.0031
32.4	3	50	0.0908	0.0228	0.1174	6	0.0004
32.4	3	100	0.0642	0.0129	0.1155	9	0.0003

Volume fraction (VF), number of clusters (#CL), number of inclusions (#INC), inclusion diameter (ID), minimum permissible distance between inclusions (MPD), diameter of cluster (CLD), number of inclusions in cluster (#INC CL), minimum permissible distance between inclusions in cluster (MPD CL).

• *Triple cluster hard core model (Clus-3)*. This model is generated in the same way as the single cluster model with three predetermined cluster locations.

2.2. Dirichlet tessellations in microstructural discretization and characterization

Dirichlet tessellation is defined as a subdivision of a region, determined by a set of points, such that each point has associated with it a region that is closer to it than to any other. These regions are termed Voronoi cells and may be identified as the basic structural elements of a heterogeneous microstructure. If $P_1(x_1), P_2(x_2), \dots, P_n(x_n)$ denote a set of n random points in a bounded region W , the interior of a Voronoi cell associated with the i th labeled point P_i is the region D_i defined as

$$D_i = \{x \in W : |x - x_i| < |x - x_j|, \forall j \neq i, P_j \in W\}. \quad (1)$$

The aggregate of all such regions D_i constitutes the Dirichlet tessellation in a plane, as shown in Fig. 1. Each region may be perceived of as the intersection of open half planes bounded by the perpendicular bisectors of lines joining the point P_i with each of its neighbors P_j . A 2D mesh generator has been developed for plane section of multiphase materials in Ref. [34], where automatic discretization into basic structural elements is based on information on the domain boundary, and the location, shape and size of the heterogeneities. Effects of the reinforcement shape and size are accounted for by a surface based tessellation algorithm, where edges of Voronoi cells

are generated for points on the surface of the heterogeneity.

Tessellation of a microstructure into Voronoi cells is of considerable significance in generating geometric descriptors to quantify a given morphology. It naturally identifies regions of immediate influence for each heterogeneity, and also its neighbors corresponding to edges of the Voronoi cells. This facilitates evaluation of parameters like the local area fractions, near neighbor and nearest neighbor distances and orientations, which are essential in quantitative characterization of the microstructure.

2.3. Statistical analysis of computer generated microstructures

Microstructural morphology for heterogeneous materials may be appropriately characterized by functions of shapes, sizes and spatial distributions of the second phase. To classify spatial distributions, it is important to identify functions and methods that can distinguish between regular, random, nonregular, nonrandom or clustered patterns. Important studies in quantitative metallography by Richmond and co-workers [24, 25], Pyrz [30, 31] and Everett and Chu [28, 29] have suggested quantification of the nature of inter-inclusion/second phase distributions as a means of characterizing microstructural morphology. The quantified functions are compared with known distribution functions for random or regular distributions to bring out the distinction, and serve as a divider between aggregated and more regular patterns. For example, Richmond and

co-workers [24, 25] have considered the distribution of nearest neighbor distances, and mean distances from near neighbors, in categorizing microstructural patterns. Everett [29] has effectively used radial distribution functions or RDFs for stereological analysis of patterns to classify actual composite microstructures. Pyrz [30–32] has also suggested investigations by various distance based parameters or by tessellation cell related parameters. He has concluded that the second order intensity function $K(r)$, which is similar in significance to RDFs, is the most informative descriptor of dispersion patterns. In the light of arguments in stereological studies, a number of geometric descriptors as suggested in Refs [24, 25, 29–31] are considered for the patterns in Fig. 1.

2.3.1. Mean and standard deviation of microstructural parameters for various patterns. For each microstructural pattern, the statistical mean and standard deviation of the local area fraction and near neighbor distances are computed and tabulated in Table 2. The local area fraction is measured as the ratio of the area of the inclusion size to that of the associated Voronoi cell. Near neighbor distances are determined as the distance between centers of inclusions that share a common Voronoi cell edge. The average number of near neighbors for each pattern (AVNUMR) increases with the number of inclusions. This average is, however, always less than 6, which is the average number of Voronoi edges for a purely Poisson distribution of points. The mean local area fractions (MAF) for all distribution

patterns are always larger than the overall mean area fraction for the RME. For hard core patterns at all volume fractions, the mean local area fraction does not change significantly with the number of inclusions, and the standard deviation (SDAF) is considerably smaller than the mean. The mean local area fraction increases with clustering, indicating dominance of area fractions in the clusters. A relatively large scatter in values is reflected by an increased standard deviation. The mean near-neighbor distance (MNND) between centers on the other hand, decreases with increased clustering especially at smaller area fractions. Concurrently, the standard deviation (SDNND) increases. MNND also decreases with an increase in the number of inclusions. Following the proposition made in Spitzig *et al.* [24], deviation from complete randomness is also investigated through two ratios, MRNND and VRNND, shown in Table 2. MRNND corresponds to the ratio of the observed mean nearest neighbor distance to the expected mean for a purely random Poisson point distribution, and VRNND is the corresponding ratio of variances. The expected mean $E(\bar{r})$ and variance $E(s^2)$ of nearest neighbor distances for the Poisson distribution are established in the literature [24, 28] as

$$E(\bar{r}) = 0.4 \left(\frac{N}{A} \right)^{-1/2}, \quad E(s^2) = \frac{4 - \pi}{4\pi} \left[\frac{2}{N/A} \right]$$

where N/A is the area density of points. For relatively small volume fractions (approximately 5%),

Table 2. Local measures characterizing the microstructural morphology

VF (%)	#CL	#INC	MAF	SDAF	AVNUMR	MNND	SDNND	MRNND	VRNND
10.8	0	25	0.1131	0.0224	4.56	0.1592	0.0171	1.5918	0.1065
10.8	0	50	0.1125	0.0212	5.00	0.1206	0.0106	1.6984	0.0828
10.8	0	100	0.1169	0.0287	5.30	0.0800	0.0095	1.6003	0.1310
10.8	1	25	0.1524	0.1083	4.72	0.1438	0.0474	1.4382	0.8207
10.8	1	50	0.1755	0.1408	5.12	0.1048	0.0383	1.4758	1.0742
10.8	1	100	0.1676	0.1151	5.44	0.0684	0.0216	1.3680	0.6836
10.8	3	25	0.1501	0.0802	4.72	0.1207	0.0419	1.2066	0.6388
10.8	3	50	0.1726	0.1299	5.24	0.0903	0.0363	1.2713	0.9666
10.8	3	100	0.1988	0.1562	5.46	0.0658	0.0265	1.3169	1.0265
21.6	0	25	0.2231	0.0394	4.56	0.1659	0.0140	1.6589	0.0713
21.6	0	50	0.2249	0.0425	5.04	0.1182	0.0103	1.6654	0.0779
21.6	0	100	0.2260	0.0445	5.30	0.0817	0.0076	1.6348	0.0840
21.6	1	25	0.2453	0.0971	4.64	0.1632	0.0298	1.6321	0.3256
21.6	1	50	0.2386	0.0794	5.12	0.1163	0.0177	1.6386	0.2289
21.6	1	100	0.2403	0.0883	5.32	0.0830	0.0127	1.6598	0.2349
21.6	3	25	0.2376	0.0755	4.80	0.1495	0.0300	1.4954	0.3285
21.6	3	50	0.2448	0.0890	5.12	0.1105	0.0242	1.5565	0.4272
21.6	3	100	0.2440	0.0936	5.32	0.0797	0.0143	1.5940	0.3001
32.4	0	25	0.3414	0.0706	4.56	0.1699	0.0189	1.6987	0.1308
32.4	0	50	0.3323	0.0515	5.00	0.1177	0.0062	1.6580	0.0284
32.4	0	100	0.3344	0.0558	5.22	0.0841	0.0061	1.6827	0.0553
32.4	1	25	0.3400	0.0747	4.64	0.1615	0.0132	1.6154	0.0634
32.4	1	50	0.3455	0.0868	5.00	0.1189	0.0122	1.6747	0.1094
32.4	1	100	0.3354	0.0601	5.30	0.0853	0.0070	1.7069	0.0729
32.4	3	25	0.3514	0.0935	4.56	0.1619	0.0124	1.6191	0.0565
32.4	3	50	0.3420	0.0792	5.00	0.1184	0.0164	1.6682	0.1971
32.4	3	100	0.3385	0.0688	5.28	0.0836	0.0082	1.6716	0.0995

Volume fraction (VF), number of clusters (#CL), number of inclusions (#INC), mean local area fraction (MAF), standard deviation of local area fraction (SDAF), average number of near neighbors (AVNUMR), mean center-to-center near neighbor distance (MNND), standard deviation of near neighbor distance (SDNND), observed mean/expected mean nearest neighbor distance (MRNND), observed variance/expected variance (VRNND).

deviations of the ratio of means (MRNND) and the ratio of variances (VRNND) from unity are known to distinguish random sets from clusters. Microstructures considered in this paper, however, have much larger volume fractions, and the relationship proposed in Ref. [24] do not hold exactly. Specifically, the value of the MRNND for all volume fractions is found to be greater than unity. Nevertheless, values of the MRNND decrease with increased clustering, a trend that is expected for clusters in a superimposed background of random points. This trend is much stronger at the lower volume fractions. Values of the VRNND on the other hand are less than unity, except for clustered patterns at low volume fractions. This indicates clusters in a background of random distribution. At higher volume fractions the distinction between hard core and clusters is less acute, as seen in the pattern diagrams.

2.3.2. Cumulative distribution and probability density functions. The cumulative distribution function $F(x)$ represents the probability that a random variable X , e.g. the local area fraction or nearest neighbor distance, assumes a value smaller than or equal to x . The probability density function $f(x)$ refers to the probability of a variable X assuming a value x and is expressed as $f(x) = dF(x)/dx$. For nearest and near neighbor distances in actual materials, Pyrz [30] has evaluated these functions to yield conclusive information about the distributions, while those for real materials have been plotted in Spitzig *et al.* [24]. Cumulative distribution and probability density functions of the local area fraction and nearest neighbor distance are plotted for all the microstructures, and a few are depicted in Figs 2 and 3. The cumulative distribution is normalized with respect to the total number of inclusions in the unit square domain.

Local Area Fraction (A)

Figures 2(a), (c), (e) and (g) shows the cumulative distribution functions $F(A)$, and Fig. 2(b), (d), (f) and (h) shows the density distribution functions $f(A)$ for 25 and 100 inclusions at 10.8% and 32.4% volume fractions, respectively. At lower volume fractions with 25 inclusions, $F(A)$ shows significant differences between the hard core (HC) and each of the clustered (Clus-1 and Clus-3) patterns, especially with an increase in the local area fraction, which increases considerably with increased clustering due to a wider dispersion. The high spikes in the density distribution function $f(A)$ for the HC pattern at 10.8% VF [Fig. 2(b)] are consequences of the steep gradients due to pronounced uniformity in the local area fraction. Intensity of spikes in $f(A)$ diminishes with clustering, reflecting lower gradients in $F(A)$. The difference in $F(A)$ for the two clustered patterns reduces as the number of inclusions increases to 100 [Fig. 2(c)]. This is indicative of a similarity in local area fraction distribution for higher inclusion concentration. The HC pattern is, however, quite different in Fig. 2(c)

and Fig. 2(c), (d). The difference between the HC and clustered patterns for $F(A)$ and $f(A)$ plots sharply reduces as the volume fraction is increased to 32.4%, indicating relatively less distinction between distributions at this VF.

Center-to-Center Nearest Neighbor Distance (d)

Figures 3(a), (c), (e) and (g) show the cumulative distribution functions $F(d)$, while Fig. 3(b), (d), (f) and (h) show the density distribution functions $f(d)$ for 25 and 100 inclusions at 10.8% and 32.4% VF, respectively. As with local area fractions, the distinction between $F(d)$ and $f(d)$ for the three patterns diminishes with increasing VF and increasing inclusion concentration. The near neighbor distance in the clusters is significantly lower than that in the HC patterns seen in Fig. 3(a). The smallest distance d for Clus-3 is slightly less than that for Clus-1. The plateau in $F(d)$, and consequently the zero values in $f(d)$, for the clustered patterns correspond to relatively large distances for which a near neighbor does not exist. This plateau decreases with higher VFs and inclusions. Spikes in $f(d)$ correspond to the number of neighbors at nearly similar distances, and the wide plateaus correspond to uniformly increasing distances. With increase in inclusion number at lower VFs, the distinction between the clustered patterns diminishes but the difference with HC remains. At 32.4% VF with 25 inclusions, $F(d)$ and $f(d)$ for the HC pattern have prolonged tails due to large near neighbor distances. The difference in lowest values of d is, however, reduced and relatively narrower plateaus occur at shorter distances in clustered patterns. All patterns possess similar tails as the number of inclusions increases to 100.

2.3.3. Second order intensity function and pair distribution function. The second order intensity function $K(r)$ has been demonstrated to be one of the most informative descriptors of morphological patterns by Pyrz [30, 31], because of its sensitivity to local perturbations in otherwise similar distributions. It has the significance of a radial distribution function [29] and is defined as the number of additional points or inclusion centers expected to lie within a distance r of an arbitrarily located point, divided by point density. For observations within a finite window W of area A , $K(r)$ corrected due to edge effects may be expressed as (see Ref. [30])

$$K(r) = \frac{A}{N^2} \sum_{k=1}^N \frac{I_k(r)}{R_p} \quad (2)$$

where N is the number of points in W , $I_k(r)$ is the number of points in the circle with center at one of the points and radius r , and R_p is the ratio of the circumference of a circle of radius r inside W to the entire circumference. Construction of the $K(r)$ function is illustrated in Fig. 4. For a given r , $I_k(r)$ is calculated for each inclusion by counting the

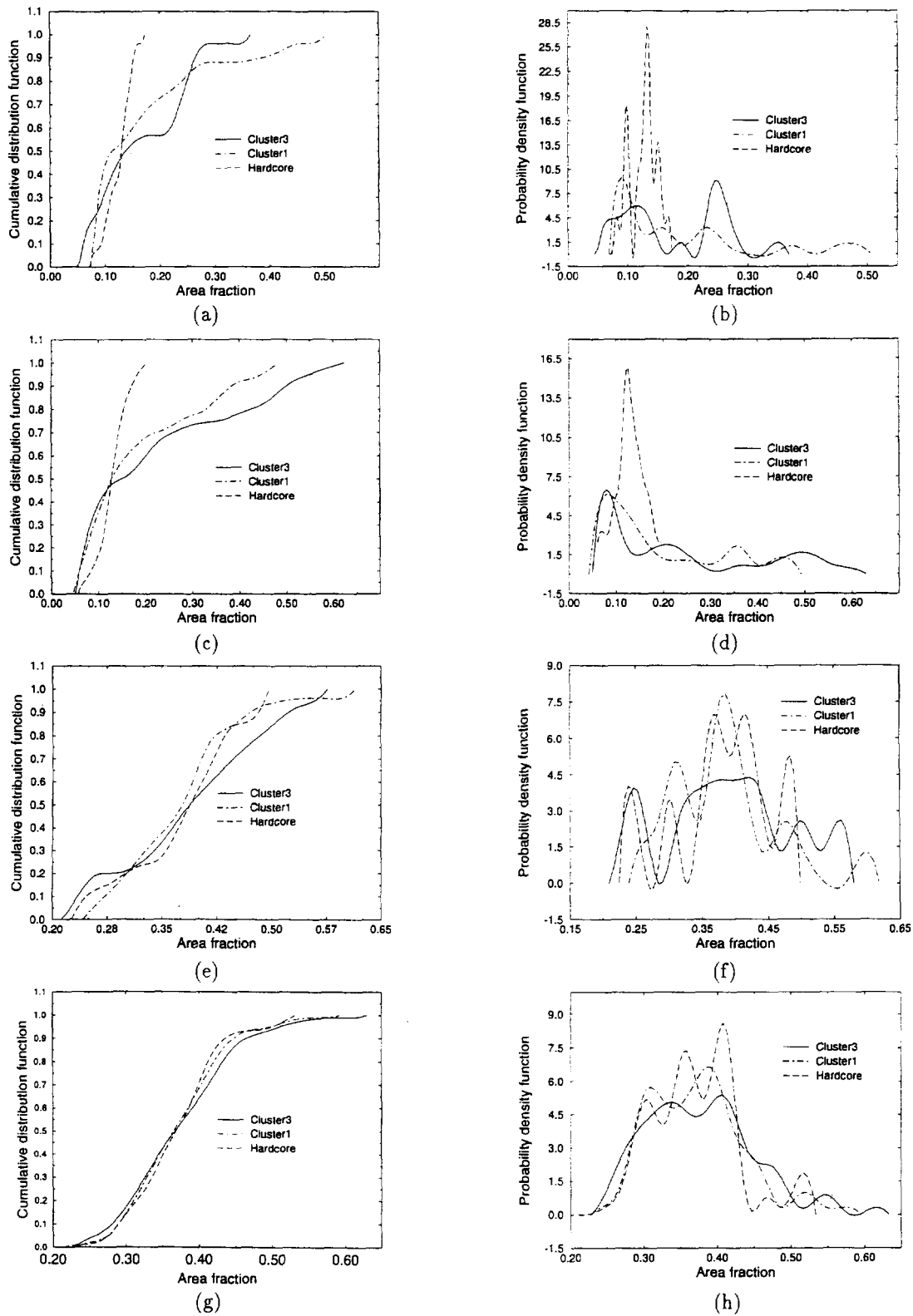


Fig. 2. Cumulative distribution functions and probability density distribution functions for local area fraction: (a) and (b) for 25 inclusions at 10.8% VF, (c) and (d) for 100 inclusions at 10.8% VF, (e) and (f) for 25 inclusions at 32.4% VF, (g) and (h) for 100 inclusions at 32.4% VF.

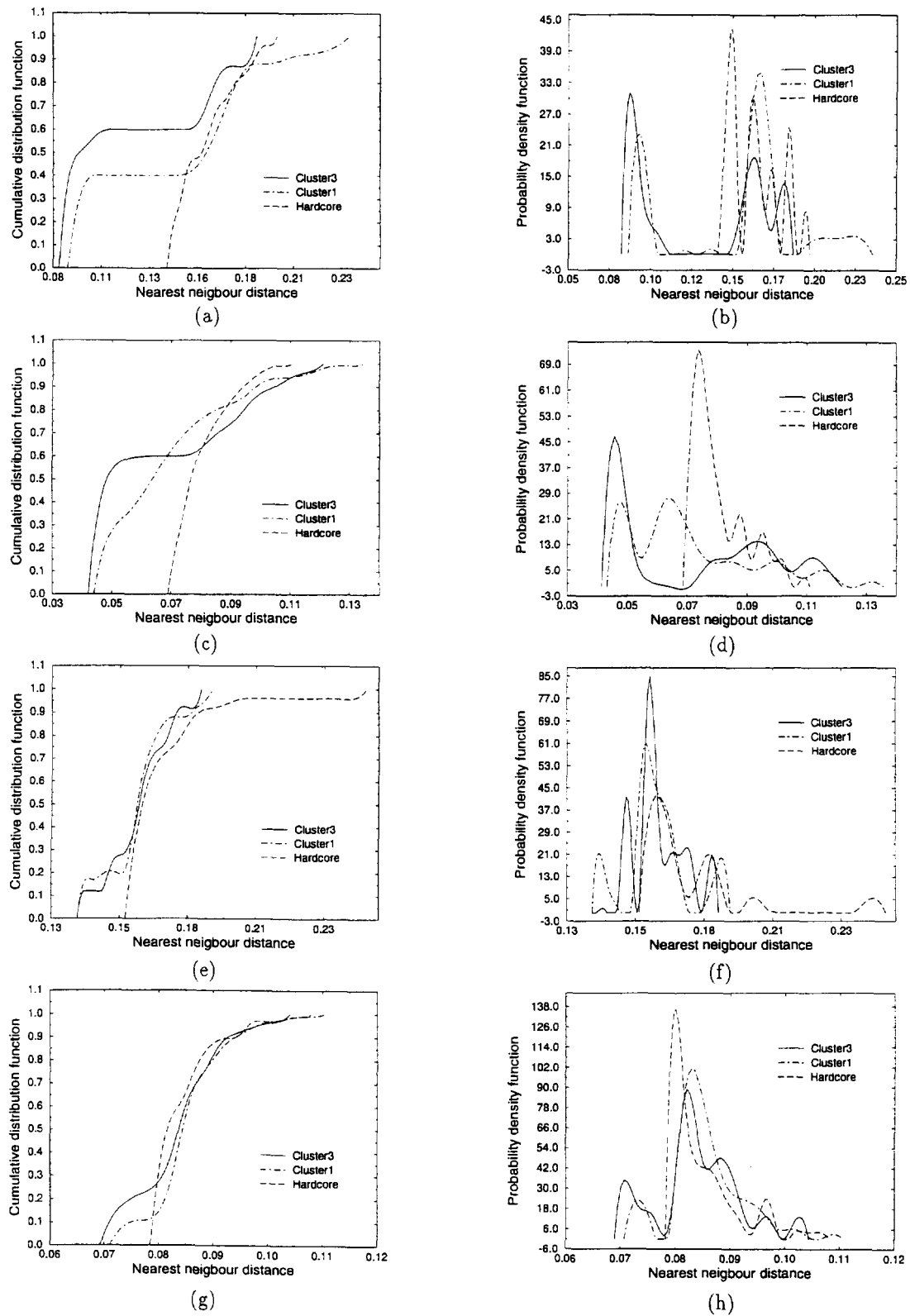


Fig. 3. Cumulative distribution functions and probability density distribution functions for nearest neighbor distance: (a) and (b) for 25 inclusions at 10.8% VF, (c) and (d) for 100 inclusions at 10.8% VF, (e) and (f) for 25 inclusions at 32.4% VF, (g) and (h) for 100 inclusions at 32.4% VF.

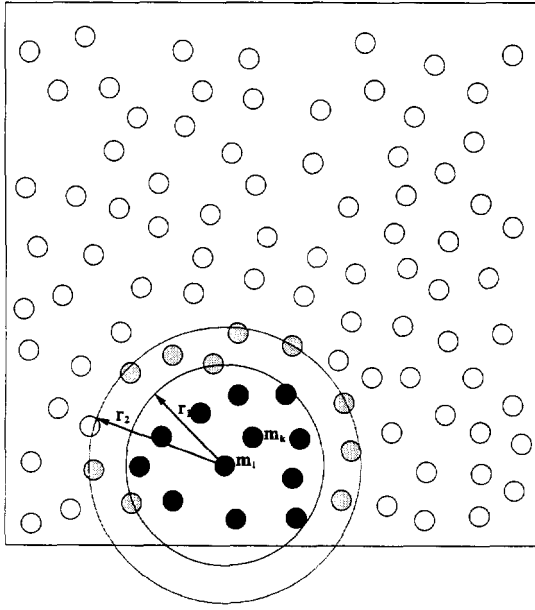


Fig. 4. Schematic diagram for generating the second order intensity $K(r)$ and marked correlation $M(r)$ functions.

number of additional inclusion centers that lie within a concentric circle of radius r around the inclusion. For example, $I_k(r)$ is 11 in Fig. (4) for $r = r_1$. For circles protruding beyond the RME window, $I_k(r)$ is divided by R_p to compensate for the bounded domain. The procedure is repeated for all inclusions at each value of r to obtain $K(r)$ by equation (2). Values of $K(r)$ for various distributions may be compared with that for a pure Poisson distribution of points, known to be πr^2 . The pair distribution function $g(r)$, on the other hand, corresponds to the probability $g(r) dr$ of finding an additional point within a circle of radius dr and centered at r , where two points are located at $r = 0$ and $r = r$, respectively. This is mathematically expressed as

$$g(r) = \frac{1}{2\pi r} \frac{dK(r)}{dr}. \quad (3)$$

Once $K(r)$ is plotted as a function of r , $dK(r)/dr$ is numerically evaluated to obtain $g(r)$. Contrary to $K(r)$, which discriminates between patterns, $g(r)$ quantifies the likelihood of occurrence of near neighbor distances. For a pure Poisson pattern, $g(r)$ assumes a unit value, signifying equal likelihood in occurrence of near neighbor distances. Figures 5 and 6 illustrate $K(r)$ and $g(r)$ plots for all microstructural patterns considered, as r varies from 0 to approximately a third of the window size.

At lower VFs (10.8%) and a low inclusion concentration (25), $K(r)$ for the clustered patterns lie above that for the Poisson pattern and diverges from

it when clustering increases. The hard core pattern, though, remains mostly below the Poisson curve, on account of the additional nonpenetrability constraint. As the VF increases (21.6 and 32.4%) for the same number of inclusions, the distinction between nonclustered and clustered patterns diminishes as seen in Figs 5(d) and (g). Divergence from the Poisson pattern is much less pronounced for the clusters. It is interesting to note that the minimum inter-inclusion distance for clustered patterns approaches the corresponding distance for hard core patterns 0.1375 at higher VFs. With larger inclusion populations (50 and 100), $K(r)$ for hard core patterns tends to be larger than that for Poisson patterns for a much larger range of r , with reduced minimum inter-inclusion distance (0.1163 for 50 and 0.0788 for 100 inclusions). This indicates that as the inclusion size decreases, so do the near-neighbor distances for the hard core patterns. As seen from Fig. 5(i) at high VF and inclusion number, it is virtually impossible to distinguish between patterns and the $K(r)$ is larger than that for the Poisson distribution for a large range of r .

From $g(r)$ plots in Fig. 6, observations made with $K(r)$ are further enhanced. Local maxima indicate that the most frequent distances and local minima correspond to the least frequent distances between patterns. For example, peaks in $g(r)$ at low r values are very pronounced for the Clus-3 pattern at 10.8% VF [Fig. 6(a), (b) and (c)]. A distance close to 0.09 is frequently observed in Clus-3 and Clus-1 distributions, but its intensity of occurrence is significantly larger for the former distribution. These spikes indicate that the frequencies in clustered patterns are very high compared with the Poisson pattern at low r 's, but are much reduced at higher r 's. Difference in frequencies between patterns are minimal at high VFs with a high inclusion population [Fig. 6(i)]. Also, as with the $K(r)$ function, the minimum r for the hard core pattern decreases with increase in inclusions. It is interesting to note from Fig. 6(d), (a) that the peak frequencies reduce from 10.8% to 21.6% VF, and increase again at 32.4% VF.

3. MICRO-MECHANICAL MODELING WITH VDFEM

3.1. The Voronoi Cell Finite Element Model (VCFEM)

The Voronoi Cell finite element method for small deformation elastic-plastic analysis of heterogeneous materials has been successfully developed in Refs [19–21], and is briefly presented here. Consider a typical representative material element Y , tessellated into N Voronoi cells. The matrix phase in each Voronoi cell Y_c is denoted by Y_m and the heterogeneity is denoted by Y_c . The matrix-heterogeneity interface ∂Y_c has an outward normal \mathbf{n}^c , while

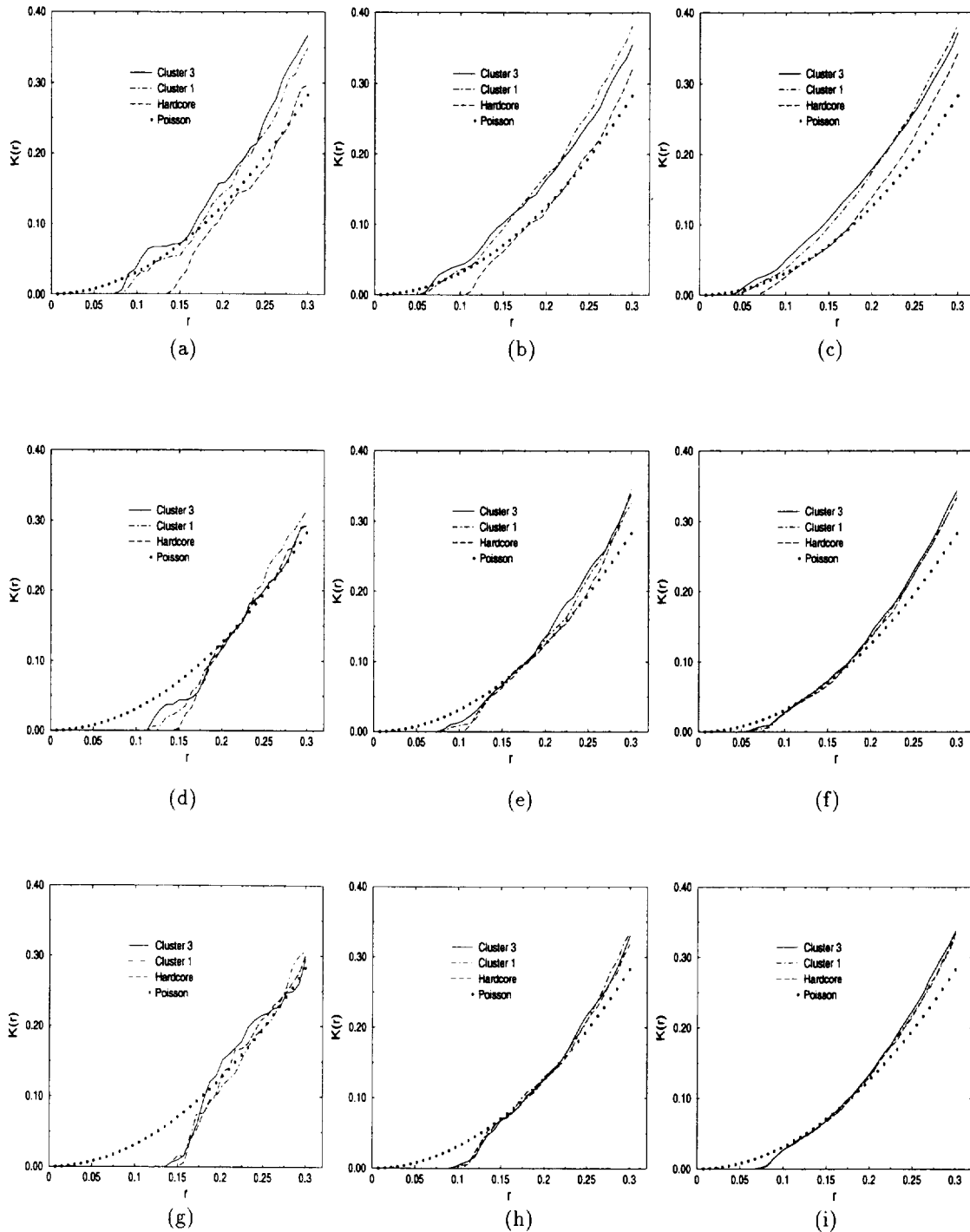


Fig. 5. Second order intensity function $K(r)$ for: (a) 25 inclusions at 10.8% VF, (b) 50 inclusions at 10.8% VF, (c) 100 inclusions at 10.8% VF, (d) 25 inclusions at 21.6% VF, (e) 50 inclusions at 21.6% VF, (f) 100 inclusions at 21.6% VF, (g) 25 inclusions at 32.4% VF, (h) 50 inclusions at 32.4% VF, (i) 100 inclusions at 32.4% VF.

\mathbf{n}^e is the outward normal to the element boundary ∂Y_e . In an incremental finite element formulation for rate independent plasticity, let $\boldsymbol{\sigma}$ be an equilibrated stress field with a strain field $\boldsymbol{\epsilon}(\boldsymbol{\sigma}, \text{load history})$, and let \mathbf{u} be a compatible displacement field on the element boundary at the beginning of an increment.

Also let $\Delta \boldsymbol{\sigma}$ correspond to an equilibrated stress increment in T_e , $\Delta \mathbf{u}$ to a compatible displacement increment on ∂Y_e , and $\Delta \mathbf{f}$ to a traction increment on the traction boundary Γ_{tm} . The incremental problem is solved by using a two field assumed stress hybrid variational principle, derived from an element energy

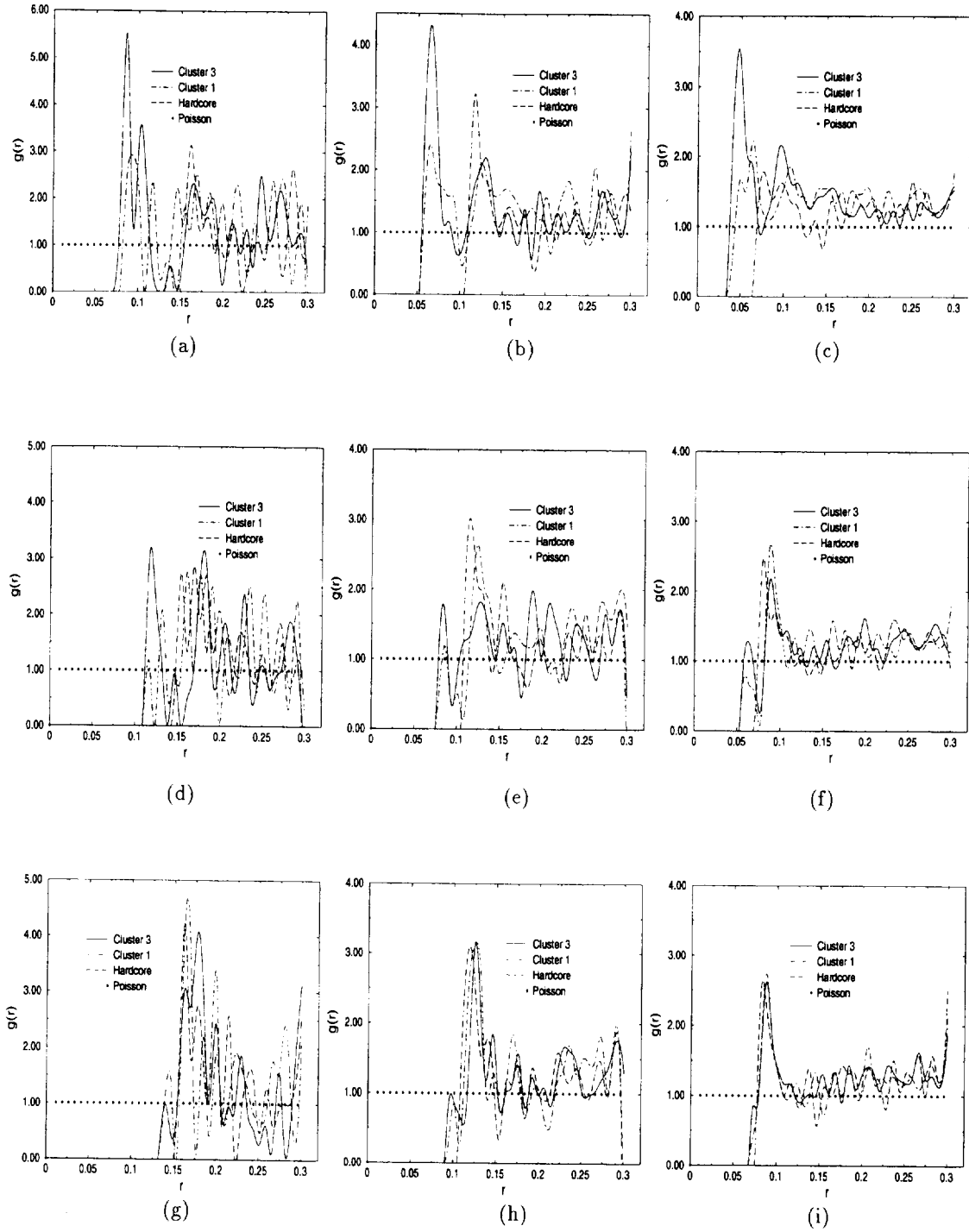


Fig. 6. Pair distribution function $g(r)$ for: (a) 25 inclusions at 10.8% VF, (b) 50 inclusions at 10.8% VF, (c) 100 inclusions at 10.8% VF, (d) 25 inclusions at 21.6% VF, (e) 50 inclusions at 21.6% VF, (f) 100 inclusions at 21.6% VF, (g) 25 inclusions at 32.4% VF, (h) 50 inclusions at 32.4% VF, (i) 100 inclusions at 32.4% VF.

functional as

$$\begin{aligned} \Pi_c(\Delta\sigma, \Delta\mathbf{u}) = & - \int_{\Gamma_c} \Delta B(\sigma, \Delta\sigma) dY - \int_{\Gamma_c} e : \Delta\sigma dY \\ & + \int_{\Gamma_c} (\sigma + \Delta\sigma) \cdot \mathbf{n}^c \cdot (\mathbf{u} + \Delta\mathbf{u}) \partial Y \end{aligned}$$

$$\begin{aligned} & - \int_{\Gamma_{int}} (\bar{\mathbf{t}} + \Delta\bar{\mathbf{t}}) \cdot (\mathbf{u} + \Delta\mathbf{u}) d\Gamma \\ & - \int_{\Gamma_c} (\sigma^m + \Delta\sigma^m - \sigma^c \\ & - \Delta\sigma^c) \cdot \mathbf{n}^c \cdot (\mathbf{u}' + \Delta\mathbf{u}') \partial Y \end{aligned} \quad (4)$$

where $\Delta \mathbf{u}^i$ is the displacement of the interface and $\Delta \mathbf{B}$ is the increment in element complimentary energy. Superscripts m and c correspond to variables in the matrix and the heterogeneity within each Voronoi cell element. The energy functional for the entire domain is obtained by adding each element functional at $\Pi = \sum_{e \in \mathcal{E}} \Pi_e$. Independent assumptions on stress increments $\Delta \boldsymbol{\sigma}$ are made in the matrix and the heterogeneity using stress functions $\Phi(\mathbf{x}, \mathbf{y})$, which result in stress expressions as

$$\{\Delta \boldsymbol{\sigma}^{m,c}\} = [\mathbf{P}^{m,c}(\mathbf{x}, \mathbf{y})] \{\Delta \boldsymbol{\beta}^{m,c}\} \quad (5)$$

where the $\{\Delta \boldsymbol{\beta}\}$'s correspond to a set of yet undetermined stress coefficients and $[\mathbf{P}]$ is a matrix of interpolation functions. To add to the element efficiency, stress functions are chosen to account for the shape of the heterogeneity near the interface, and also to facilitate traction reciprocity at the interface. Compatible displacement increments on the element boundary ∂Y_e as well as on the interface ∂Y_c , are generated by interpolation in terms of generalized nodal values. The displacement increments on the element boundary and interface may then be written as

$$\{\Delta \mathbf{u}^{e,c}\} = [\mathbf{L}^{e,c}] \{\Delta \mathbf{q}^{e,c}\} \quad (6)$$

where $\{\Delta \mathbf{q}^e\}$ and $\{\Delta \mathbf{q}^c\}$ are generalized displacement increment vectors on ∂Y_e and ∂Y_c , and $[\mathbf{L}]$ is an interpolation matrix. Substituting element approximations for stresses (5) and displacements (6), in the energy functional (4), and setting the first variations with respect to the stress coefficient $\Delta \boldsymbol{\beta}^m$ and $\Delta \boldsymbol{\beta}^c$ respectively to zero, results in the following two weak forms of the kinematic relationships:

$$\begin{aligned} \int_{Y_m} [\mathbf{P}^m]^T \{e + \Delta e\} dY &= \int_{\Gamma_{Y_c}} [\mathbf{P}^m]^T [\mathbf{n}^c] [\mathbf{L}^c] dY \{\Delta \mathbf{q}\} \\ &\quad - \int_{\Gamma_{Y_c}} [\mathbf{P}^m]^T [\mathbf{n}^c] [\mathbf{L}^c] dY \{\Delta \mathbf{q}^c\} \\ \int_{Y_c} [\mathbf{P}^c]^T \{e + \Delta e\} dY &= \int_{\Gamma_{Y_c}} [\mathbf{P}^c]^T [\mathbf{n}^c] [\mathbf{L}^c] dY \{\Delta \mathbf{q}^c\}. \end{aligned}$$

Setting the first variation of the total energy functional with respect to $\Delta \mathbf{q}$ and $\Delta \mathbf{q}^c$ to zero, results in the weak form of the traction reciprocity conditions as

$$\sum_{e=1}^N \left[\begin{array}{c} \int_{\Gamma_{Y_c}} [\mathbf{L}^c]^T [\mathbf{n}^c]^T [\mathbf{P}^m] dY \quad \mathbf{0} \\ - \int_{\Gamma_{Y_c}} [\mathbf{L}^c]^T [\mathbf{n}^c]^T [\mathbf{P}^m] dY \quad \int_{\Gamma_{Y_c}} [\mathbf{L}^c]^T [\mathbf{n}^c]^T [\mathbf{P}^c] dY \end{array} \right] \left\{ \begin{array}{c} \beta^m + \Delta \beta^m \\ \beta^c + \Delta \beta^c \end{array} \right\} = \sum_{e=1}^N \left\{ \begin{array}{c} \int_{\Gamma_{Y_m}} [\mathbf{L}^e]^T \{\mathbf{f} + \Delta \mathbf{f}\} dY \\ \{\mathbf{0}\} \end{array} \right\}. \quad (8)$$

For a rate independent elastic-plastic material following J_2 flow theory, the nonlinear finite element equations (7) and (8) are solved for the stress parameter increments $(\Delta \boldsymbol{\beta}^m, \Delta \boldsymbol{\beta}^c)$ and nodal displacement increments $(\Delta \mathbf{q}, \Delta \mathbf{q}^c)$.

3.2. Asymptotic homogenization for multiple scale analysis

In real heterogeneous materials, dimensions of the RME are typically very small in comparison with the dimensions of the body, and the ratio of microscopic and macroscopic scales is represented by a very small positive number ϵ . A high level of heterogeneity in the microstructure causes a rapid variation in evolutionary variables like deformation and stresses in a small neighborhood ϵ of a macroscopic point \mathbf{x} . This corresponds to a microscopic scale ($\mathbf{y} = \mathbf{x}/\epsilon$) and consequently all variables are assumed to exhibit dependence on both length scales, i.e. $\Phi^e = \Phi(\mathbf{x}, \mathbf{x}/\epsilon)$. In homogenization theory [19, 22], a periodic repetition of the microstructure about a macroscopic point \mathbf{x} is assumed. For small deformation elastoplasticity, the periodic displacement rate in an RME (\mathbf{Y}) is approximated by an asymptotic expansion with respect to parameter ϵ :

$$\begin{aligned} \dot{\mathbf{u}}(\mathbf{x}) &= \dot{\mathbf{u}}^0(\mathbf{x}, \mathbf{y}) + \epsilon \dot{\mathbf{u}}^1(\mathbf{x}, \mathbf{y}) + \epsilon^2 \dot{\mathbf{u}}^2(\mathbf{x}, \mathbf{y}) \\ &\quad + \dots, \quad \mathbf{y} = \frac{\mathbf{x}}{\epsilon}. \end{aligned} \quad (9)$$

From the rate form of the constitutive equation, the stress rate tensor $\dot{\boldsymbol{\sigma}}_y$ can then be expressed as

$$\dot{\boldsymbol{\sigma}}_y = \frac{1}{\epsilon} \dot{\boldsymbol{\sigma}}_y^0 + \dot{\boldsymbol{\sigma}}_y^1 + \epsilon \dot{\boldsymbol{\sigma}}_y^2 + \epsilon^2 \dot{\boldsymbol{\sigma}}_y^3 + \dots \quad (10)$$

Substituting in the rate equilibrium equation, the microscopic kinematic and equilibrium equations may be delineated as

$$\dot{\boldsymbol{\sigma}}_y^1 = \dot{\boldsymbol{\sigma}}_y^{kl}(\mathbf{y}) \frac{\partial \dot{\mathbf{u}}_k^0}{\partial x_l}, \quad \dot{\mathbf{u}}_i^1 = \chi(\mathbf{y})_i^{kl} \frac{\partial \dot{\mathbf{u}}_k^0}{\partial x_l} \quad (\text{kinematics}) \quad (11)$$

and

$$\frac{\partial \dot{\boldsymbol{\sigma}}_y^{kl}(\mathbf{y})}{\partial y_j} = 0 \quad (\text{equilibrium}). \quad (12)$$

In equation (11), $\dot{\boldsymbol{\sigma}}_y^{kl}$ is a \mathbf{Y} -antiperiodic function and χ^{kl} is a \mathbf{Y} -periodic function representing characteristic modes of the RME. From equation (11) the microscopic constitutive relations are written as

$$\dot{\boldsymbol{\sigma}}_y^{kl}(\mathbf{y}) = E_{ijpm} \left[T_{pm}^{kl} + \frac{\partial \chi_p^{kl}}{\partial y_m} \right] \quad (13)$$

where E_{ijkl} is the constituent tangent modulus and T_{ij}^{kl} is a fourth order identity tensor. The mean of equation (13) yields the homogenized elastic-plastic

tangent modulus, for use in the macroscopic analysis, in the form

$$\begin{aligned} E_{ijkl}^H &= \langle \hat{\sigma}_{ij}^{kl} \rangle = \frac{1}{|\mathbf{Y}|} \int_Y \hat{\sigma}_{ij}^{kl} dY \\ &= \frac{1}{|\mathbf{Y}|} \int_Y E_{ijpm}^e \left(T_{pm}^{kl} + \frac{\partial Y_p^{kl}}{\partial Y_m} \right) dY. \end{aligned} \quad (14)$$

The mean of equations in \mathbf{Y} yields the macroscopic form of the governing and constitutive equations for the elastic-plastic heterogeneous material as

$$\begin{aligned} \frac{\partial \hat{\Sigma}_{ij}}{\partial X_j} &= -f_i \quad \text{in } \Omega_{\text{structure}} \\ \hat{\Sigma}_{ij} &= E_{ijkl}^H \dot{\epsilon}_{kl} \end{aligned} \quad (15)$$

where $\Omega_{\text{structure}}$ corresponds to the macroscopic domain, $\hat{\Sigma} (= \langle \hat{\sigma}^l \rangle)$ and $\dot{\mathbf{u}}^0$ are the averaged macroscopic stress rate tensor and the displacement rate, respectively.

3.3. Incorporation in a macroscopic analysis module

The microscopic Voronoi cell finite element module is incorporated in a macroscopic analysis module ABAQUS, with the interface for homogenized material properties created through the user-prescribed subroutine UMAT in ABAQUS. The resulting analysis code is called VCFEM-HOMO. The material constitutive relation at each integration point of macroscopic ABAQUS elements is input through homogenization, from the microscopic VCFEM analysis with periodicity boundary conditions. The VCFEM module is executed to evaluate microscopic stress increments $\Delta \hat{\sigma}^l$, and the instantaneous homogenized tangent modulus E_{ijkl}^H from given values of macroscopic strain $\hat{\epsilon} + \Delta \hat{\epsilon}$, as detailed in Ref. [19].

4. STRESS ANALYSIS AND EFFECTIVE PROPERTIES

Numerical simulations are conducted for all the generated microstructures with the multiple scale finite element code VCFEM-HOMO. The 2D analysis for evolution of elastic-plastic stress-strains and overall properties is restricted to plane strain. Material properties are for an $\text{Al}_2\text{O}_3/\text{Al}$ composite, where the Al_2O_3 fiber is assumed to be elastic while the aluminum matrix is an elastic-plastic material with the following properties:

99% crystalline α -alumina (Al_2O_3) coated with silica fiber: Young's Modulus (E_c) = 344.5 GPa, Poisson's ratio (ν_c) = 0.26.

2 wt% Li-Al binary alloy matrix: Young's Modulus (E_m) = 68.9 GPa, Poisson's ratio (ν_m): 0.32, initial yield stress (Y_0): 94 MPa, post yield flow rule:

$$\epsilon_{\text{eqv}} = \frac{Y_0}{E_m} \left\{ \frac{\sigma_{\text{eqv}}}{Y_0} \right\}^5.$$

4.1. Elastic-plastic analysis of various microstructures

Each of the 27 microstructures is subjected to an overall macroscopic strain of 1% in the horizontal direction. Contour plots of Von Mises stresses and effective plastic strains at the end of loading are depicted for a few representative realizations in Fig. 7. Stresses are uniformly high in all brittle inclusions of the hard core pattern. However for clustered patterns, inclusion stresses within clusters are considerably higher than those elsewhere. Also, the overall stress levels rise with clustering. Effective plastic strains are concentrated near the inclusion-matrix interface and are distributed uniformly for hard core patterns. For clustered patterns, however, they are significantly higher inside clusters.

4.2. Anisotropy from geometric and response considerations

The majority of constitutive methods for heterogeneous materials assume isotropy in macroscopic response. This leads to a considerable difference between the experimentally observed and simulated behavior of structures. Microstructural morphology has a strong effect on directional dependence in material behavior. Since the constituent material properties are individually isotropic, a strong correlation is expected between anisotropies arising from geometric dispersion and mechanical response. In this section, two geometric measures for detecting anisotropy are verified against the anisotropic elastic tangent moduli obtained from the VCFEM-HOMO analysis. These descriptors for identifying anisotropy in nonrandom-dispersions are discussed next.

4.2.1. Angular position of nearest neighbor. Histograms depicting the angular relationship between a baseline and the vector joining nearest neighbors, has been proposed as a qualitative measure of the anisotropic distribution in Refs [24, 35]. While the angular distribution is expected to be nearly uniform for a Poisson pattern due to equal likelihood of all angles, dominance of certain angular orientations will prevail in some aligned patterns. Figure 8 depicts a few representative histograms covering a range from 0 to 90°, with subranges of 10°. The histograms may be intuitively classified into a few general patterns, viz.

(a) *Uniform distribution (UD).* The frequency of nearest neighbor occurrence is roughly uniform for all 10° subranges, indicating a near isotropic distribution of inclusions. For example, Fig. 8(a) (25 inclusions, 21.6% VF, HC) and Fig. 8(g) (100 inclusions, 32.4% VF, Clus-3) are among the various patterns that exhibit this behavior.

(b) *Random distribution (RD).* For this set of histograms, the frequency of occurrence of nearest neighbors varies randomly for all angles, and hence they suggest a nonpreferential overall dispersion. Random angular dispersions are predominantly

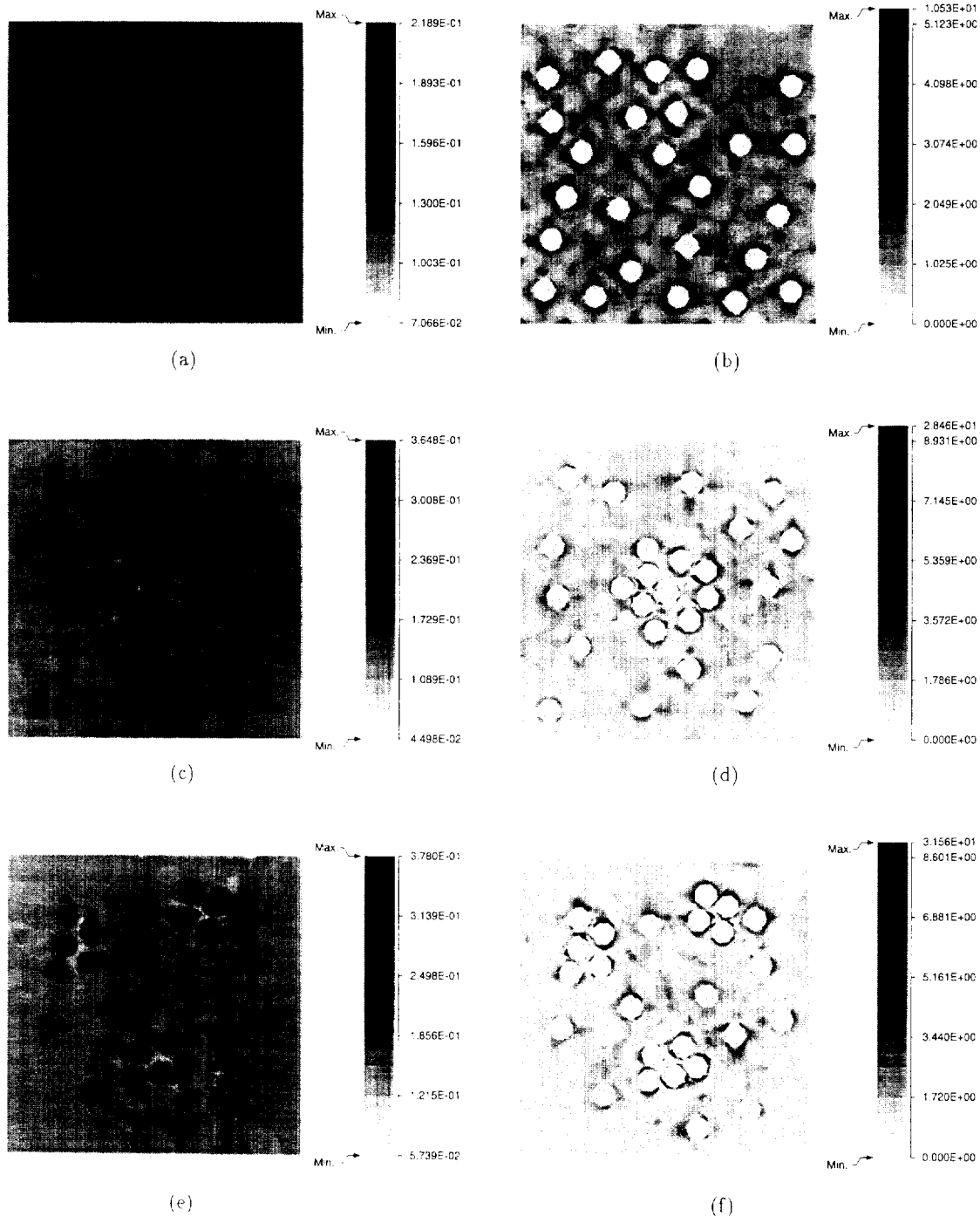


Fig. 7. Von Mises stress (in GPa) and effective plastic strain distribution at 1% overall strain, for 25 inclusions at 10.8% volume fraction: (a) and (b) HC pattern, (c) and (d) Clus-1 pattern, (e) and (f) Clus-3 pattern.

observed in lower VFs (10.8%) and a lower number of inclusions (25) for all levels of clustering. This is shown in Fig. 8(b) (25 incls, 10.8% VF, HC) and Fig. 8(c) (25 incls, 10.8% VF, Clus-3).

(c) *Strong preferred orientation (SPO)*. Dominance of a single angular orientation due to a preferred alignment of inclusions in a particular direction

describes this set of histograms. This anisotropic behavior is characterized by spikes of large numbers of inclusions at given angles, and is generally observed in microstructures with fewer inclusions (25) and a higher VF (32.4%), as depicted in Fig. 8(d) (25 incls, 32.4% VF, HC), Fig. 8(e) (25 incls, 32.4% VF, Clus-1), and Fig. 8(f) (25 incls, 32.4% VF, Clus-3).

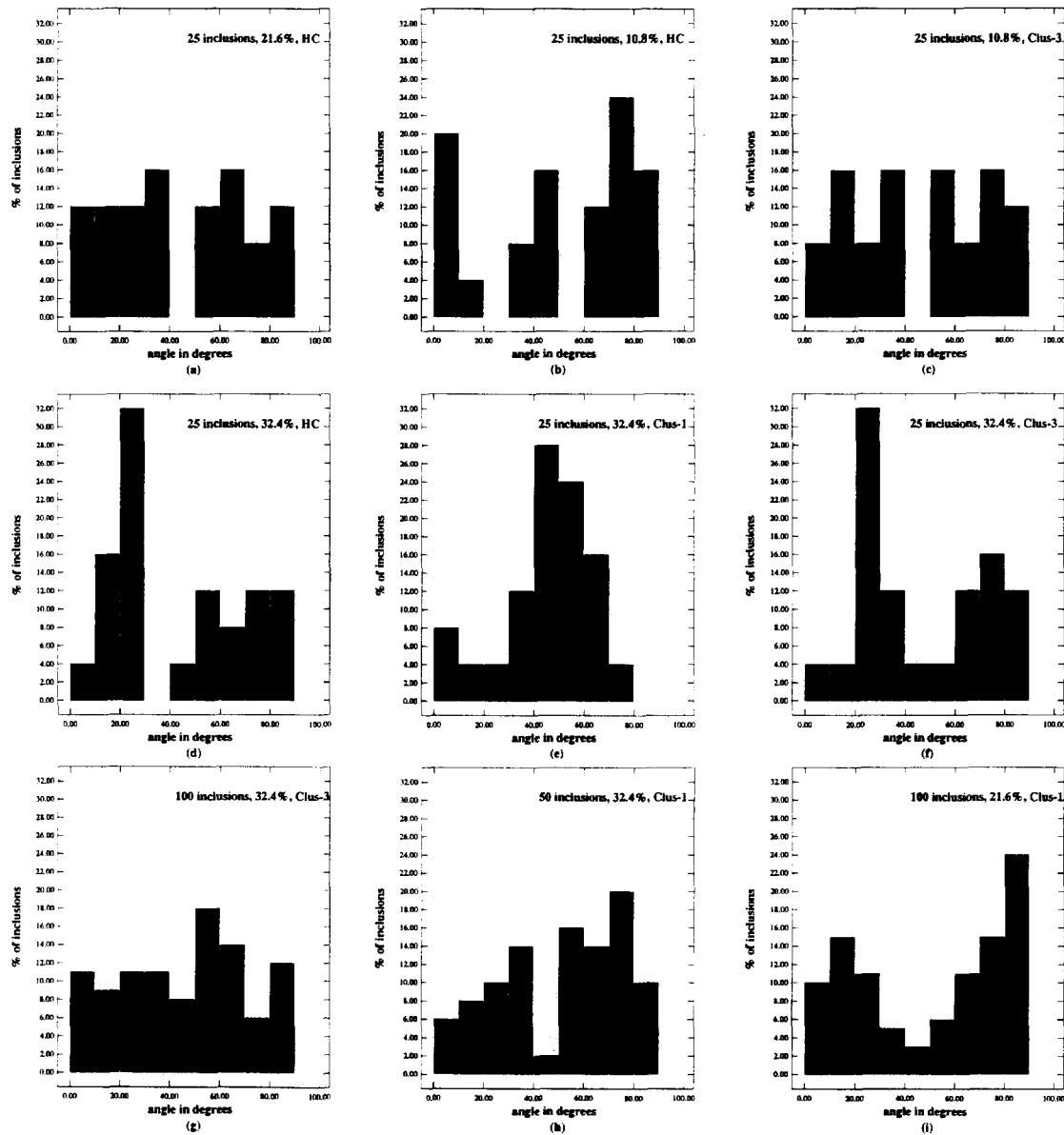


Fig. 8. Histogram of angular relationship between nearest-neighbors of inclusions.

(d) *Gradually increasing preferred orientation (GIPO)*. This morphology exhibits a gradual transition towards a preferred orientation and is characterized by continuously increasing or decreasing graded histograms. It is a strong indicator of anisotropic dispersion, and is frequently observed in larger inclusion concentration (50–100) and higher VF (21.6–32.4%) microstructures with clustering, as illustrated in Fig. 8(h) (50 incls. 32.4% VF, Clus-1) and Fig. 8(i) (100 incls. 21.6% VF, Clus-1).

Due to a lack of quantitative delineation, intuitive classification of all patterns into the categories mentioned above is presented as ANG in Table 3. Isotropy in dispersion is generally observed for patterns at lower volume fractions. At moderate VFs, anisotropy increases with the number of inclusions,

while for high VFs, it is predominant for the single cluster patterns.

4.2.2. Mean Intercept Aspect Ratio ($MAR = a_{\text{mean}}/b_{\text{mean}}$). A measure of the anisotropy defined as the ratio of mean intercept lengths in two orthogonal directions was introduced in Refs [24, 25]. In this section, the above definition has been modified to accommodate intercept variations at different orientations. Intercept lengths are determined at uniform 10° angular increments by measuring the length of a line that passes through the inclusion centroid, between cell edges at this orientation. The intercepts are averaged for all Voronoi cells in the microstructures. The mean intercept lengths are then plotted as a function of angle (0–360°). An equivalent ellipse is subsequently constructed by equating the zeroth, first

Table 3. Local parameters characterizing overall anisotropy of microstructure

VF (%)	#CL	#INC	ANG	MAR	A_{xx}	A_{yy}	OI1	OI2	OI3
10.8	0	25	RD	1.0757	0.99807	0.99987	1.00026	1.00014	0.99832
10.8	0	50	RD	1.0500	0.99882	1.00019	0.99963	0.99980	0.99848
10.8	0	100	RD	1.0380	0.99867	0.99975	1.00050	1.00027	0.99913
10.8	1	25	RD	1.1113	0.99720	0.99986	1.00029	1.00015	0.99747
10.8	1	50	RD	1.1218	0.99665	1.00013	0.99975	0.99987	0.99642
10.8	1	100	UD	1.0268	0.99821	0.99983	1.00035	1.00019	0.99853
10.8	3	25	RD	1.0718	0.99823	1.00022	0.99957	0.99978	0.99783
10.8	3	50	SPO	1.1238	0.99749	0.99980	1.00039	1.00020	0.99785
10.8	3	100	GIPO	1.0407	0.99997	0.99913	1.00174	1.00091	1.00158
21.6	0	25	UD	1.0963	0.99799	1.00216	0.99569	0.99765	0.99412
21.6	0	50	SPO	1.0513	0.99386	0.99967	1.00067	1.00036	0.99446
21.6	0	100	GIPO	1.0309	0.99932	0.99975	1.00049	1.00022	0.99977
21.6	1	25	RD	1.0585	0.99783	1.00075	0.99849	0.99918	0.99647
21.6	1	50	GIPO	1.0433	0.99730	0.99722	1.00558	1.00387	1.00233
21.6	1	100	GIPO	1.0686	0.99062	0.99806	1.00388	1.00209	0.99408
21.6	3	25	RD	1.0563	0.99477	0.99898	1.00205	1.00111	0.99660
21.6	3	50	UD	1.0407	0.99569	0.99902	1.00197	1.00108	0.99745
21.6	3	100	GIPO	1.0315	0.99637	1.00059	0.99881	0.99936	0.99530
32.4	0	25	SPO	1.0520	0.99248	0.99836	1.00329	1.00186	0.99534
32.4	0	50	GIPO	1.0463	0.98882	0.99798	1.00404	1.00228	0.99233
32.4	0	100	GIPO	1.0489	0.98907	0.99842	1.00316	1.00178	0.99181
32.4	1	25	SPO	1.0414	0.99734	1.00226	1.00069	1.00039	0.99978
32.4	1	50	GIPO	1.0329	0.99874	0.99795	1.00412	1.00233	1.00235
32.4	1	100	SPO	1.0250	1.00339	1.00456	0.99091	0.99348	0.99543
32.4	3	25	SPO	1.0549	0.98262	1.00031	0.99939	0.99965	0.98210
32.4	3	50	SPO	1.0822	0.98557	1.00407	0.99190	0.99541	0.97861
32.4	3	100	UD	1.0357	0.99175	1.00504	0.98997	0.99253	0.98312

Volume fraction (VF), number of clusters (#CL), number of inclusions (#INC), angular orientation index (ANG), mean aspect ratio ($MAR = L_{mean}^{mean} / L_{mean}^{mean}$), anisotropy index in xx -direction ($A_{xx} = E_{xxxx}^H / E_{xxxx}^{isotr}$), anisotropy index in xy -direction ($A_{xy} = E_{xyxy}^H / E_{xyxy}^{isotr}$), orthotropy index ($OI1 = E_{xyxy}^H / E_{xxxx}^H$), orthotropy index ($OI2 = E_{zzzz}^H / E_{zzzz}^{isotr}$), orthotropy index ($OI3 = E_{xyxy}^H / 0.5(E_{xxxx}^H - E_{zzzz}^H)$).

and second moments of the actual plot to those of the ellipse. For each ellipse the ratio of the major axis to the minor axis ($MAR = a_{mean}/b_{mean}$) is then computed and is tabulated in Table 3. For an isotropic distribution of inclusions this ratio (MAR) is expected to be unity. The mean difference in MAR from unity is calculated to be 0.0577 with a standard deviation of 0.028. A deviation value of 0.045 from unity (which is lower than the mean) is intuitively selected as a criterion to differentiate between isotropic and anisotropic patterns. A comparison of inferences from the intercept aspect ratio with that from the angular position reveals that though the two measures concur for many microstructural morphologies, they also differ in a few cases. For example, isotropy at lower VFs is dominant for the ANG classification but is not so strong with this descriptor. For higher VFs, more agreement exists between the two measures.

4.2.3. Effective tangent modulus E_{ijkl}^H . The homogenized elastic tangent modulus E_{ijkl}^H in equation (14) is obtained as an orthotropic tensor from VCFEM-HOMO. Various distinguishing parameters are evaluated for determining the degree of anisotropy resulting from dispersion of the heterogeneities. Presented in Table 3, these may be subdivided into two classes, viz.

(a) *Deviation from isotropic material properties.* Equivalent isotropic components of the elasticity tensor, e.g. Lamé constants are evaluated by equating strain energies for the orthotropic and idealized isotropic materials. Two equations needed for the

Lamé constants are obtained for conditions of (i) biaxial stretching corresponding to a hydrostatic loading state and (ii) biaxial tension-compression corresponding to a deviatoric loading state. Anisotropy indices $A_{xx} = E_{xxxx}^H / E_{xxxx}^{isotr}$ and $A_{xy} = E_{xyxy}^H / E_{xyxy}^{isotr}$ are ratios of the respective components in the orthotropic tensor to the idealized isotropic tensor. To distinguish between isotropy and anisotropy, a deviation measure $DEV1 = (1 - \frac{1}{2}\{A_{xx} + A_{xy}\})$ is selected. If $DEV1 \leq 0.001$, then the response is intuitively classified as isotropic. It is emphasized that this measure is chosen arbitrarily to create a distinction, and is not a conclusive dividing line between anisotropy and isotropy. It is generally observed that this measure yields anisotropy with clustering (Clus-1 and Clus-3), especially at low and moderate VFs. Anisotropy is dominant at higher VFs for all patterns.

(b) *Deviation from isotropic behavior.* Orthotropy indices $OI1 = E_{xyxy}^H / E_{xxxx}^H$, $OI2 = E_{zzzz}^H / E_{zzzz}^H$ and $OI3 = E_{xyxy}^H / 0.5(E_{xxxx}^H - E_{zzzz}^H)$ represent the behavioral deviation of the homogenized orthotropic elasticity tensor from isotropy. For this case also, the deviation measure $DEV2 = (1 - \frac{1}{3}\{OI1 + OI2\})$, if ≤ 0.001 , intuitively classifies the behavior as isotropic. According to this measure, isotropy dominates at lower VFs while anisotropic behavior rules at higher VFs.

Comparison of all the four measures indicates that the geometric measures (1) and (2) concur in 44% of all cases, and response measures (3a) and (3b) agree with each other in 67% of all cases. Inference from

all measures concur in more than a third of all cases, and three out of four measures produce the same conclusion in approximately 67% of all cases. In general, criterion (2) is found to agree more with (3a), which is considered to be a good indicator of anisotropic behavior.

4.3. Marked correlation and probability density functions for stresses

An important criterion in determining length scales that characterize a microstructural representative material element (RME), is the influence of local morphology on the microscopic stress/strain distribution. These stress/strain levels and distributions are sensitive to perturbations in local morphology, and consequently functions that distinguish between their variations for different microstructural patterns can provide important insights on the microstructure-property correlations. Pyrz [31] has introduced a novel “marked correlation function” for multivariate characterization of patterns, by associating field variables, e.g. stresses, with each particle in a heterogeneous domain. A mark may correspond to any feature associated with a point or heterogeneity in the domain. The marked correlation function for a heterogeneous domain A containing N inclusions is mathematically expressed as [31, 36]

$$M(r) = \frac{\frac{dH(r)}{dr}}{g(r)}$$

where

$$H(r) = \frac{1}{m^2} \frac{A}{N^2} \sum_i \sum_{k=1}^N m_i m_k(r). \quad (16)$$

Here m_i denotes a mark or a variable associated with the i th inclusion, k^i is the number of inclusions which have their centers within a circle of radius r around the i th inclusion, m_k are the marks for those inclusions, and m is the mean of all marks. $H(r)$ is termed the mark intensity function and $g(r)$ is the pair distribution function. From its definition, $M(r)$ establishes a relationship between the position and the associated variables for heterogeneities.

From considerations of microscopic evolution, the marks are identified with each of the four state variables, viz. (a) the maximum principal stress in each inclusion, (b) the maximum principal stress, (c) the maximum hydrostatic stress and (d) the maximum Von Mises stress in the matrix region, for regions associated with each inclusion. The associated region corresponds to the interior of each Voronoi cell. The maximum values are evaluated from values at several sampling points within each Voronoi cell. The construction of $M(r)$ follows from that of $K(r)$ as shown in Fig. 4. For every r , $m_k(r)$ in equation (16) is evaluated for each inclusion by associating each inclusion with the maximum stress value in that Voronoi cell, from which $H(r)$ is

evaluated. $H(r)$ is then plotted as a function of r and numerically differentiated to obtain $M(r)$ in equation (16). Plots of $M(r)$ for 10.8% VF with 25 inclusions and 32.4% VF with 100 inclusions are illustrated in Fig. 9(a)–(f). Uniform $M(r)$ plots of unit value occur for regular patterns, and correspond to identical marks for all inclusions. Comparison of various state variables indicates that the matrix hydrostatic stress possesses the strongest mark as illustrated by its difference from unity, while marks for matrix Von Mises stresses are the weakest. The marks for Von Mises stresses are mostly insensitive to the distance r and are not of much consequence. It is interesting to note that variables (a), (b) and (c) exhibit very similar $M(r)$ characteristics. The highest value of $M(r)$ occurs at the minimum r , implying that the distances of neighboring inclusions have a strong effect on the mark intensities. At a distance r_{inter} , where $M(r)$ nearly decays to unity, separation between heterogeneities cease to have a significant influence on variables. Such information leads to conclusions about the size of the RME. Figure 9(a), (b) and (c) shows that the intensity of marks in stresses are much higher for the clustered patterns, and the highest occur for the Clus-1 pattern. The triple cluster Clus-3 pattern has the largest mark at higher VFs. At low VFs (10.8%) the undulations do not stabilize at near unit values, and hence the critical influence region r_{inter} extends beyond the range of r considered. This influence region is seen to shrink with increasing inclusion concentration, especially at higher VFs, as seen in Fig. 9(d), (e) and (f). The Clus-3 pattern quickly stabilizes at the unit value, thereby settling for a smaller RME. The dips near the end are due to the window edge effect and may be ignored.

Figure 10 shows the density distribution functions $f(\sigma)$ at 10.8% VF with 25 inclusions and at 32.4% VF with 100 inclusions. The distinction between the $f(\sigma)$ for the three patterns diminishes with increasing VF and increasing inclusion numbers. At a lower VF with less inclusions, the HC pattern has a considerably large probability density over a rather small range of stresses. This indicates that the variation in stresses for this pattern is low. Stress values for clustered patterns are significantly higher than that for the HC pattern as implied by the tails. The probability density peak decreases with increased clustering. Among the three patterns shown, the maximum principal stress in the inclusion shows the maximum difference in the $f(\sigma)$ plots. The distinction between the $f(\sigma)$'s decreases with increased VF and inclusion numbers.

5. CONCLUSIONS

Tessellation of heterogeneous domains into Voronoi cells that represent basic structural elements has important implications in both quantitative metallography and modeling of microstructures. This paper is intended to establish the unified tools of

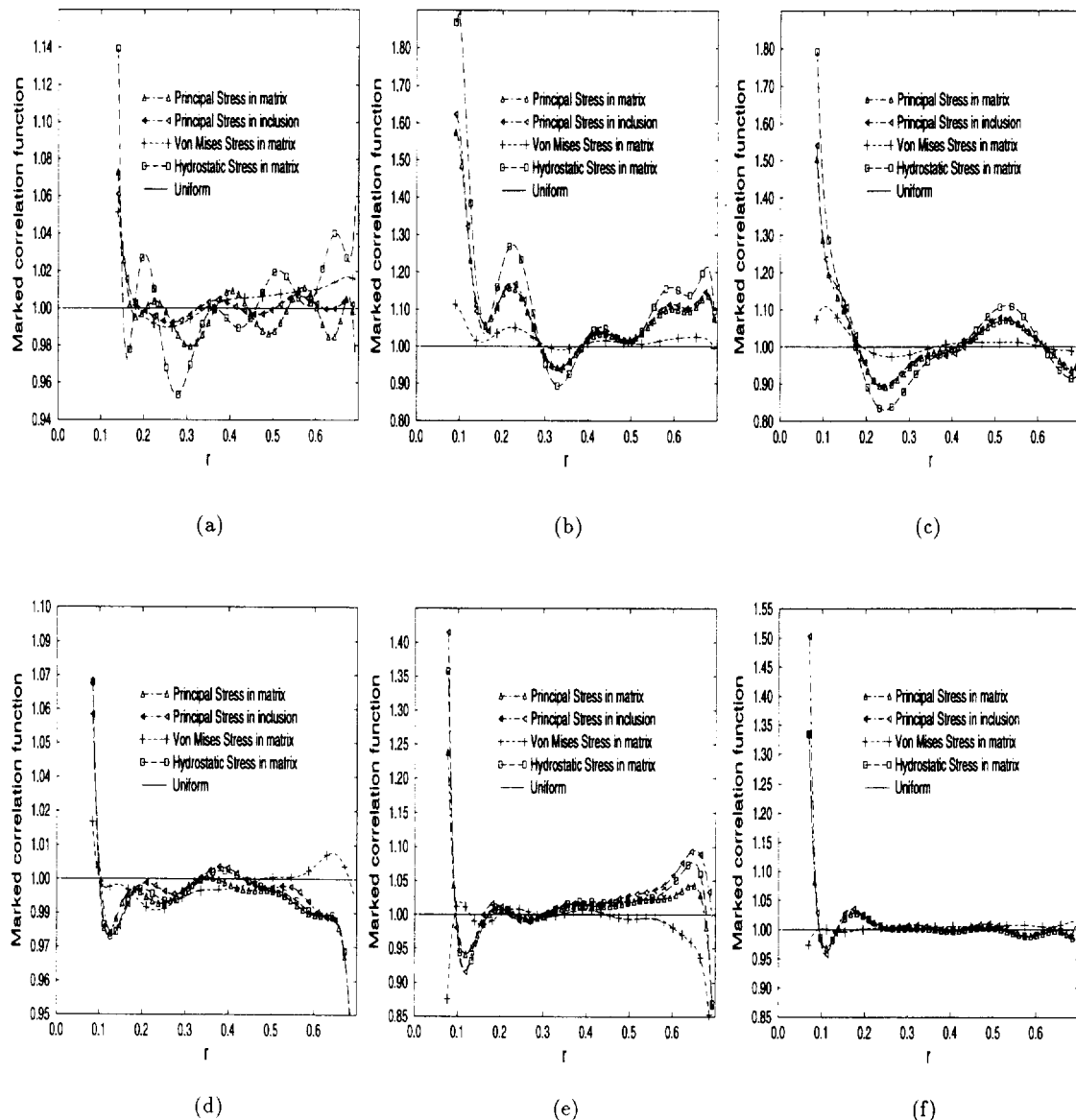


Fig. 9. Marked correlation function $M(r)$ for: 25 inclusions at 10.8% VF, (a) HC, (b) Clus-1, (c) Clus-3; 100 inclusions at 32.4% VF, (d) HC, (e) Clus-1, (f) Clus-3.

Voronoi cell based characterization and finite element modeling for studying various aspects of micromechanics. In particular, it investigates correlations between functions representing the morphology and mechanical response of various microstructures. A total of 27 different microstructures are computer simulated to represent a wide range of clustering, heterogeneity concentration and volume fractions. These are tessellated into Voronoi cells to study the effects of variation in geometric constructs on stereologic information and on mechanical behavior. Parameters like local area fraction and nearest neighbor distance, together with geometry description functions like mean and standard deviations, cumulative and probability density functions, radial distribution functions, etc.,

are utilized for microstructural characterization from qualitative and quantitative points of view. Both the probability functions F and f , and intensity functions K and g are quite effective in qualitatively distinguishing patterns at low volume fractions especially with less heterogeneities. At higher volume fractions the distinction between these patterns diminishes, and then the functions lose their effectiveness. The cumulative and density distribution functions of local area fraction [$F(A)$ and $f(A)$] and nearest neighbor distance [$F(d)$ and $f(d)$] are both reasonably effective at low volume fractions for the range of particle numbers considered. The intensity and pair distribution functions $K(r)$ and $g(r)$ are, however, seen to be most effective for lower inclusion numbers at the low volume fractions.

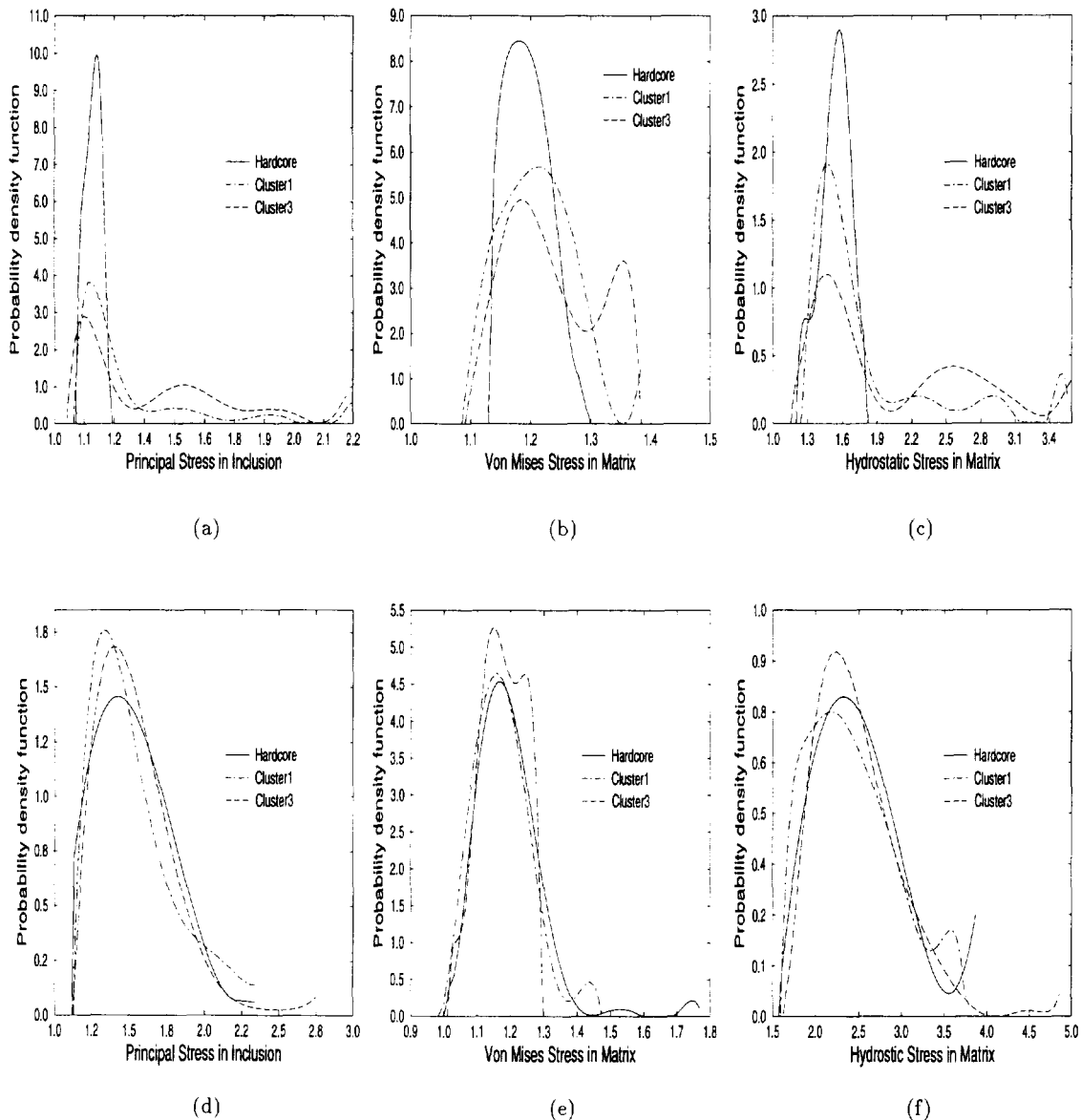


Fig. 10. Probability density distribution functions for stresses; 10.8% VF for 25 inclusions (a) maximum principal stress in inclusion, (b) maximum Von Mises stress in matrix, (c) maximum hydrostatic stress in matrix, and 32.4% VF for 100 inclusions (d) maximum principal stress in inclusion, (e) maximum Von Mises stress in matrix, (f) maximum hydrostatic stress in matrix.

The Voronoi cell FEM is effectively used to perform small deformation elastic-plastic stress analysis for all the microstructures generated. Contour plots clearly indicate that stresses inside, and plastic strains at the interface of brittle inclusions located within the clusters, far exceed their counterparts outside clusters. Anisotropy in geometry and mechanical response anisotropy is gauged by various orientation and tangent modulus based estimators. This study shows that moderate agreement exists in predictions by the geometric and response descriptors, and good conformity is seen within each class. It may be generally concluded that the hard core patterns at low and moderate volume fractions are generally anisotropic, but clustering shows strong

signs of anisotropy at all volume fractions. Interesting observations on the correlation between morphological distributions and the influence regions for stress manifestations, are made through the marked correlation function. This function for Von Mises stress in the matrix is found to be least affected by dispersion patterns, while it is quite sensitive for principal stresses and matrix hydrostatic stress. Finally, the probability density distributions for the various stresses match the observations for geometric parameters like A and d .

Observations made in this study are sufficiently conclusive and may be used with confidence in characterization and modeling of actual heterogeneous materials, where the shape and size may also

vary with location. This study is currently under way and will be reported in future papers.

Acknowledgements—This work has been sponsored by the Mechanics and Materials program (Program Director O. Dillon) of the National Science Foundation through an NSF Young Investigator grant (Grant No. CMS-9457603), and by the Ohio State University Center for Advanced Materials and Manufacturing of Automotive Components (CAMMAC). Computer support by the Ohio Supercomputer Center through grant #PAS813-2 is also gratefully acknowledged.

REFERENCES

1. Brockenbrough, J. R., Suresh, S. and Wienecke, H. A., *Acta metall. mater.*, 1991, **39**(5), 735.
2. Christman, T., Needleman, A. and Suresh, S., *Acta metall. mater.*, 1989, **37**, 3029.
3. Böhm, H. J., Rammerstorfer, F. G., Fischer, F. D. and Siegmund, T., *J. Engng. Mater. Technol. (Trans. ASME)*, 1994, **116**, 268.
4. Hashin, Z. and Strikman, S., *J. Mech. Phys. Solids*, 1963, **11**, 127.
5. Hill, R., *J. Mech. Phys. Solids*, 1965, **13**, 213.
6. Budiansky, B., *J. Mech. Phys. Solids*, 1965, **13**, 223.
7. Mori, T. and Tanaka, K., *Acta metall. mater.*, 1973, **21**, 571.
8. Tandon, G. P. and Weng, G. J., *J. appl. Mech.*, 1988, **55**, 126.
9. Dvorak, G. and Bahei-el-din, Y. A., *J. appl. Mech.*, 1982, **49**, 327.
10. Li, G. and Ponte Castenada, P., *Int. J. Solids Struct.*, 1993, **30**, 3189.
11. Milton, G. W., *J. Mech. Phys. Solids*, 1982, **30**, 177.
12. Torquato, S. and Stell, G., *J. Chem. Phys.*, 1985, **82**, 980.
13. Bao, G., Hutchinson, J. W. and McMeeking, R. M., *Acta metall. mater.*, 1991, **39**, 1871.
14. Tvergaard, V., *Acta metall. mater.*, 1990, **38**, 185.
15. Nakamura, T. and Suresh, S., *Acta metall. mater.*, 1993, **41**(6), 1665.
16. McHugh, P. E., Asaro, R. J. and Shih, C. F., *Acta metall. mater.*, 1993, **41**(5), 1461.
17. Böhm, H. J., Rammerstorfer, F. G. and Weissenbek, E., *Comp. Mater. Sci.*, 1993, **1**, 177.
18. Böhm, H. J. and Rammerstorfer, F. G., *Proc. IUTAM Symp. on Microstructure-Property Interactions in Composite Materials*, ed. R. Pyrz. Kluwer Academic Publishers, 1995.
19. Ghosh, S., Lee, K. and Moorthy, S., *Comp. Meth. Appl. Mech. Engng.*, in press.
20. Moorthy, S. and Ghosh, S., *Int. J. Num. Meth. Engng.*, 1996, in press.
21. Ghosh, S. and Moorthy, S., *Comp. Meth. appl. Mech. Engng.*, 1995, **121**, 373.
22. Ghosh, S., Lee, K. and Moorthy, S., *Int. J. Solids Struct.*, 1995, **32**(1), 27.
23. Ghosh, S. and Liu, Y., *Int. Num. Meth. Engng.*, 1995, **38**(8), 1361.
24. Spitzig, W. A., Kelly, J. F. and Richmond, O., *Metallography*, 1985, **18**, 235.
25. Wray, P. J., Richmond, O. and Morrison, H. L., *Metallography*, 1983, **16**, 39.
26. Rouns, T. N., Fridy, J. M., Lippert, K. B. and Richmond, O., *Simulation and Theory of Evolving Microstructures*, ed. M. P. Anderson and A. D. Rollet. The Minerals and Materials Soc., 1990.
27. Fridy, J. M., Rouns, T. N., Lippert, K. B., Nes, E. and Richmond, O., *Proc. 3rd Int. Conf. Aluminium Alloys*, Vol. 2, Trondheim, Norway, 1992.
28. Everett, R. K. and Chu, J. H., *J. Comp. Mater.*, 1992, **27**, 11, 1129.
29. Everett, R. K., *J. Comp. Mater.*, in press.
30. Pyrz, R., *Comp. Sci. Technol.*, 1994, **50**, 197.
31. Pyrz, R., *Mater. Sci. Engng.*, 1994, **A177**, 253.
32. Pyrz, R., *Optimal Design with Advanced Materials*, ed. P. Pedersen. Elsevier Science Publishers B.V., 1993.
33. Brockenbrough, J. R., Hunt, W. H. and Richmond, O., *Scripta metall. et mater.*, 1992, **27**, 385.
34. Ghosh, S. and Mukhopadhyay, S. N., *Comput. and Struct.*, 1991, **41**, 245.
35. Ashby, M. F. and Ebeling, R., *Trans. Am. Inst. Min. Engrs*, 1966, **236**, 1396.
36. Stoyan, D., *Math Nachr.*, 1984, **116**, 197.